Received: 13 September 2024 | Revised: 17 July 2025 | Accepted: 12 November 2025

DOI: 10.33012/navi.740

REGULAR PAPERS

Distortion-Aware Multilevel Coded Spreading Symbol Optimization for Future Navigation Signals

Florian C. Beck*[1,2] | Christoph Enneking[1] | Steffen Thölert[1,2] | Michael Meurer[1,2]

[1] Institute of Communications and Navigation
German Aerospace Center (DLR)
82234 Weßling
Germany

[2] Chair of Navigation
RWTH Aachen University
52062 Aachen
Germany

Correspondence
*Florian Beck
Münchener Str. 20
82234 Weßling
Germany
Email: florian.beck@dlr.de

Abstract

The navigation signals of global navigation satellite systems have undergone development with limited consideration given to inherent payload and receiver constraints. The forthcoming satellite generation will be equipped with flexible, fully digital payloads and feature enhanced clock architectures, which may offer potential performance improvements for positioning, navigation, and timing (PNT) users. A significant challenge is to realize these performance improvements at the user level while addressing distortions in transmitter and receiver hardware that impair PNT performance. This study reviews previous signal design concepts and extends the multilevel coded spreading symbol optimization framework to account for nonlinear and linear payload distortions and receiver band limitations. The proposed comprehensive distortion-aware optimization methodology yields signal candidates with enhanced robustness by improving performance metrics such as mean tracking error jitter and differential range bias, consequently delivering greater user benefits than signal designs optimized for minimally distortion-affected signal propagation scenarios.

Keywords

code-division multiple access, multilevel coded spreading symbol, pulse shaping, signal design

1 | INTRODUCTION

Many modern positioning, navigation, and timing (PNT) applications depend on navigation signals provided by global navigation satellite systems (GNSSs) or similar systems. These signals contain essential navigation data and, more importantly, allow ranging to highly synchronized transmitters with known locations, thus enabling PNT. In the context of GNSSs, research interest in modulation schemes and navigation signal design intensified two decades ago with efforts to modernize the Global Positioning System (GPS) and the upcoming launch of BeiDou satellite system (BDS) and Galileo (GAL) satellites. In particular for new GPS code-division multiple access (CDMA) signals, Betz and Goldstein (2002) proposed the binary offset carrier (BOC) and Hegarty et al. (2004a) proposed the binary coded spreading symbol (BCS) modulation as an upgrade for binary phase-shift keying (BPSK)-rectangular (R) signals (e.g., GPS L1 C/A or

Licensed under CC-BY 4.0 © 2026 Institute of Navigation

GPS L1 P(Y)). In follow-up studies conducted by Pratt and Owen (2003), Pratt and Owen (2004), and Hegarty et al. (2004b), the advantages in terms of ranging performance and multipath mitgation of BOC and BCS signals were confirmed. Based on these findings, Hein et al. (2005) proposed a composite BCS signal for the GAL E1 open service signals. This signal was later formalized by Ávila Rodríguez et al. (2007) and is referred to today as a CBOC modulated signal, which is a specific implementation of a MBOC modulation. The commonality of all of the aforementioned modulation techniques is that they introduce a subcarrier rate by subdividing a BPSK-R chip in uniform-duration subchips. This circumstance was formalized by Ávila Rodríguez (2008) and labeled as multilevel coded spreading symbol (MCS) modulation, which is able to capture most currently broadcast GNSS signals with strictly time-limited chip shapes with uniform subchip duration.

In the search for GAL E1 open service signals, Giugno and Luise (2005) investigated CDMA chip shaping, concluding that the band limitation imposed by the transmitter and receiver hardware is one of the most important constraints in navigation signal optimization. Even after the new GNSS signals were finalized and broadcast, Floch et al. (2010) compared signal candidates with time- and band-limited chip shapes. They determined that a systematic design approach with time-limited prolate spheroidal wave functions (PSWFs) could yield significant performance improvements compared with the existing GAL E6 BPSK-R (5) signal. Further studies from Antreich et al. (2009) and Antreich and Nossek (2011) suggested the use of band-limited PSWF-shaped signals, which can optimally concentrate signal energy within a given bandwidth, to increase the received signal power and ranging performance. Another signal optimization approach by Zhang et al. (2011b) provided a framework for increasing the ranging performance of CDMA signals through the use of a weighted orthogonal function basis for PSWF, sinusoidal offset carrier, and MCS modulated signals by maximizing the Gabor or root mean square (RMS) bandwidth (Betz, 2015), which is an inversely proportional metric for the code tracking jitter or the time of arrival (TOA) estimation error variance of the code phase (Betz & Kolodziejski, 2009).

While these studies have advanced our knowledge of navigation signal design and demonstrated increases in ranging performance under ideal conditions by providing closed-form solutions, the evolving landscape of satellite technology is calling for a recalibration of navigation signal design paradigms. It is often the case that traditional optimization methods fail to adequately account for the stochastic nature of payload and receiver tolerances and distortions, which may be induced by a number of factors including transmitter and receiver filtering, nonlinear effects of amplifiers and mixers, and so forth. The implementation of signal concepts optimized in idealized conditions may be disadvantageous in the presence of distortions, which can limit the achievable performance of these concepts in real-world transmission and reception scenarios (Beck et al., 2023). Distortions have a detrimental impact on ranging accuracy, introducing biases and spurious components that can impede the achievement of optimal performance in high-accuracy and safety-critical applications (Vergara et al., 2019). The deployment of new GNSS satellites with flexible payloads can facilitate signal designs that can adapt to real-world distortions beyond those already broadcast, such as the BPSK-R(1), BPSK-R(10), and MBOC waveforms, thereby fully exploiting the capabilities of upcoming satellite hardware and bringing improvements in transmitter clock synchronization, achieved, for instance, with optical inter-satellite

links and more stable oscillators (Dassié & Giorgi, 2021; Schuldt et al., 2021), down to the user. Another reason to explore distortion-aware navigation signal design concepts is motivated by the prospect of broadcasting additional signals by emerging low Earth orbit (LEO)-PNT systems (Reid et al., 2018) in the already congested lower and upper L-band. In the event that LEO-PNT systems transmit waveforms in the L-band that can be easily processed with existing receiver hardware (e.g., BPSK-R(1)), even with an offset to the center frequencies of already present GNSS, multiple access interference (MAI) violations are likely to occur according to radio frequency compatibility (RFC) analyses performed by Sharma et al. (2024) and Beck et al. (2024a), which may require a refinement of the International Telecommunication Union recommendation "ITU-R M.1831-1" (2015) or the deployment of more complex LEO-PNT signal designs considering MAI.

The objective of this study is to develop a framework for designing CDMA navigation signals that can effectively address the distortion issues inherent to transmitter and receiver hardware, as well as the impact of additional error sources such as multipath propagation. The framework incorporates the aspect of signal distortion and incorporates user constraints into a comprehensive optimization problem (OP). Adopting a comprehensive and flexible optimization approach to generic navigation signal design, as opposed to a fragmented approach, offers the advantage of generating an optimal and applicable solution from the outset for a particular set of constraints and distortions. This advantage can significantly benefit users who intend to employ CDMA navigation signals not only in the domain of GNSSs but also for emerging applications such as LEO-PNT or PNT on the moon. The objective of this OP is to minimize the standard deviation (SD) of the range biases, the mean of the TOA estimation error SD, or a weighted linear combination of the two objectives for a set of distortion realizations, each represented by a combination of payload and receiver characteristics (CPRC). The objective weight depends on the user type or the PNT application. The OP considers a number of parameters and is subject to a variety of constraints. These constraints include, for instance, an average transmit power constraint, a multipath rejection constraint, a limit on the level of MAI permitted with legacy GNSS and signals, and so forth. The proposed methodology enables the incorporation of this extensive array of constraints into navigation signal design. In the context of specific use cases, it may be essential to prioritize certain constraints over others.

This study extends the navigation signal optimization framework to establish a novel signal design methodology that can derive an optimized signal for various types of PNT systems that satisfy realistic constraints. The paper presents CDMA chip optimization and preliminarily explores existing MCS optimization for GNSS to mitigate the effects of distortion while satisfying user constraints, using GPS L5 data/pilot waveforms as an example. This paper serves as an extension to the work presented by Beck et al. (2024b). The results highlight the potential for significant performance improvements in GNSS ranging signals through the integration of distortion-aware optimization techniques. In the selected case study, we investigate the trade-off between two competing goals: reducing a differential range bias metric and reducing a mean code tracking error jitter metric. As an example, we present a subset of the optimized MCS selected based on multiple trade-off rationales. We find viable MCS capable of reducing either the differential range bias metric by 6.4% or the mean tracking jitter metric by 56.2%, with respect to the GPS L5 performance.

2 | SYSTEM MODEL

The objective of this section is to provide an overview of the components of the system model utilized in this work.

2.1 | Overview

To capture the distortion-affected interplay between different payloads and receivers, the system model simulates the navigation signal in baseband for K combinations of K_1 payload and K_2 receiver characteristics. The index sets $\mathcal{K}_1 = \{1, ..., K_1\}$ and $\mathcal{K}_2 = \{1, ..., K_2\}$ identify selected characteristics for a payload and receiver, respectively. Based on $\mathcal{K}_1$ and $\mathcal{K}_2$, the cross product of the sets is used:

$$\tilde{\mathcal{K}} = \mathcal{K}_1 \times \mathcal{K}_2 = \{\underbrace{(1,1)}_{:=1}, \underbrace{(2,1)}_{:=2}, ..., \underbrace{(k_1, k_2)}_{:=k}, ..., \underbrace{(K_1 - 1, K_2)}_{:=K-1}, \underbrace{(K_1, K_2)}_{:=K}\} \tag{1}$$

From this, the distortion index set $\mathcal{K} = \{1, ..., k, ..., K\}$ with $|\mathcal{K}| = K_1 K_2 := K$ is derived, which maps the indices of a CPRC to one index $k = k_1 + K_1(k_2 - 1)$. The time-invariant system model consists of a navigation signal generation unit (NSGU) with band limitation modeled via an input multiplexer (IMUX) filter $h_1(t)$, a frequency generation and up-conversion unit (FGUU) $\mathbb{U}\{.\}$, a nonlinear but memoryless high-power amplifier (HPA) model $g(.)$, an analog payload deformation represented by an output multiplexer (OMUX) filter $h_{\mathrm{O}}^{(k)}(t)$ of the k-th CPRC, a scalar path loss coefficient γ_{PL}, a down-conversion unit $\mathbb{D}\{.\}$, and a receiver front-end characteristic $h_{\mathrm{R}}^{(k)}(t)$ of the k-th CPRC. The baseband receive signal with the propagation delay $\tau_0^{(k)}$ is as follows:

$$r^{(k)}(t) = h_{\mathrm{R}}^{(k)}(t) * \mathbb{D}\left\{\sqrt{\gamma_{\mathrm{PL}}} h_{\mathrm{O}}^{(k)}(t) * g\left(\mathbb{U}\left\{h_1(t) * x\left(t - \tau_0^{(k)}\right)\right\}\right)\right\} + \xi(t) \tag{2a}$$

$$\triangleq s^{(k)}(t) + \xi(t) \quad \forall k \in \mathcal{K} \tag{2b}$$

where $\xi(t) \sim \mathcal{CN}(0, N_0)$ denotes complex receiver noise with noise density N_0 and $*$ represents the convolution operator. The following expression denotes the ideal complex transmit signal with total signal power P and modulation phases ϕ_l, $j^2 = -1$:

$$x(t) = \sqrt{P} \sum_{l=1}^{2} x_l(t) e^{j\phi_l} = \sqrt{P}\left(x_1(t) e^{j\phi_1} + x_2(t) e^{j\phi_2}\right) \tag{3}$$

We have the following:

$$x_l(t, \boldsymbol{w}_l) = \sum_{i=-\infty}^{+\infty} c_l[i] d_l[i] \sqcap \left(\frac{t - \left(i - \frac{1}{2}\right) T_{\mathrm{c}}}{T_{\mathrm{c}}}\right) p_l(t - iT_{\mathrm{c}}, \boldsymbol{w}_l) \tag{4a}$$

$$\triangleq c_l(t) d_l(t) \sum_{i=-\infty}^{+\infty} p_l(t - iT_{\mathrm{c}}, \boldsymbol{w}_l) \quad \forall l \in \mathcal{L} \tag{4b}$$

as the l-th MCS spreading waveform using the spreading waveform index set $\mathcal{L} = \{1, 2\}$, with the notation of the R-function:

$$\sqcap(t) = \begin{cases} 1 & -0.5\,\mathrm{s} \le t < +0.5\,\mathrm{s} \\ 0 & \text{else} \end{cases} \tag{5}$$

Each spreading waveform is constructed using the bipolar range code values $c_l[i] \in \{-1, +1\}$, the bipolar navigation message or secondary code bits $d_l[i] \in \{-1, +1\}$, the MCS pulse shape $p_l(t, \boldsymbol{w}_l)$ based on the weight vector $\boldsymbol{w}_l$, and T_c as the duration of a CDMA chip. The utilization of the MCS as the CDMA chip shape facilitates the implementation of well-understood and potent multiplexing methods such as Constant Envelope Multiplexing via Intermodulation Construction (Yao et al., 2017), which can handle the MCS as an input. Although the system model would be flexible enough to support other chip shapes or signal bases, this study solely explores the MCS. When employing range code sequences with minimal cross-correlation (Gold, 1967), each spreading waveform is uncorrelated with the other spreading waveform (Kaplan & Hegarty, 2005) and has a corresponding power-weighted signal replica $c_l(t)$, which is the pulsed version of the l-th range code. In this study, $x_1(t)$ is referred to as the pilot signal, which is optimized, and $x_2(t)$ is the data signal, whose optimization lies beyond the scope of this paper. Waveform staggering as explored by Vergara and Antreich (2012) lies beyond the scope of this paper.

2.2 | Two-Component Complex Baseband Signal

Most current broadcast GNSS signals fit the definition of the MCS (Ávila Rodríguez, 2008). The spreading waveform, as described by Equation (4), is constructed using an MCS:

$$p_l(t, \boldsymbol{w}_l) = \sum_{n=1}^{N_\mathrm{sc}} w_{ln} \sqcap\left(\frac{t - \left(n - \frac{1}{2}\right)T_\mathrm{sc}}{T_\mathrm{sc}}\right) = \sum_{n=1}^{N_\mathrm{sc}} w_{ln} \sqcap_n(t) \quad \forall l \in \mathcal{L} \tag{6}$$

where N_sc denotes the number of subchips, T_c denotes the CDMA chip duration, $T_\mathrm{sc} = T_\mathrm{c} / N_\mathrm{sc}$ denotes the subchip duration, and $w_{ln} \in \mathbb{R}$ is the n-th weight of the R-shaped and time-shifted n-th subchip $\sqcap_n(t)$ defined by the R-function, which constitutes the orthogonal function basis. Simple GNSS signal examples with $N_\mathrm{sc} = 1$ include GPS L1 C/A, GPS L5 (data/pilot), and GAL E5a/b. More relevant examples include any BOC or CBOC signal such as the GAL E1b/c ($N_\mathrm{sc} = 12$) and authorized services from GPS, GAL, and BDS. The proposed nomenclature for MCSs is MCS $(\boldsymbol{w}, N_f)$, where $\boldsymbol{w}$ denotes the $N_\mathrm{sc} \times 1$ weight vector and N_f is a multiplicative factor of the GNSS base frequency $f_\mathrm{b} = 1.023$ MHz, defining the chipping rate $f_\mathrm{c} = N_\mathrm{f} f_\mathrm{b}$ and subchipping rate $f_\mathrm{sc} = 1 / T_\mathrm{sc} = N_\mathrm{sc} N_\mathrm{f} f_\mathrm{b}$ (Ávila Rodríguez, 2008).

This study investigates the potential application of an MCS modulated signal in combination with a secondary signal, which may be either an already broadcast legacy waveform or an MCS modulated signal creating a constant-envelope composite signal. The inspiration for the setup is the simple but effective GPS L5 signal composed of two BPSK-R(10) waveforms. One of these waveforms is modulated in-phase (I) and the other is modulated in quadrature-phase (Q), requiring no intermodulation (IM) component. Based on this setup, the investigated composite signal is composed of one MCS pilot waveform, which is modulated I, and one data

waveform, which is modulated in Q, obtained by setting $\phi_1 = 0$ and $\phi_2 = \pi / 2$. The weights of the data waveform are chosen in two fashions, reflecting two scenarios.

2.2.1 | *Legacy Scenario: Non-Constant-Envelope Signal With the BPSK-R Data Waveform*

One possible approach is to optimize the MCS of the pilot exclusively, leaving the pulse shape of the data waveform unaltered, with the exception of a power adjustment. This scenario reflects a legacy configuration in which the data waveform remains a BPSK-R(10). For this simple setup, the two-component complex composite signal $x(t)$ power shares are defined as follows:

$$\eta_l = \frac{1}{N_{\text{sc}}} \sum_{n=1}^{N_{\text{sc}}} w_{ln}^2 \in [0,1] \quad \forall l \in \mathcal{L} \tag{7}$$

if no IM products are used. Consequently, the signal generation power shares must attain the following:

$$\eta_1 + \eta_2 = 1 \tag{8}$$

To generate a composite signal with an MCS pilot and a BPSK-R data waveform, the weights of the latter waveform are set to the following:

$$w_{2n} = \sqrt{1 - \eta_1} \quad \forall n \in \mathcal{N} \tag{9}$$

with $\mathcal{N} = \{1,...,N_{\text{sc}}\}$ such that $x(t)$ as defined in Equation (3) has an average power P. The selection of these weights results in a non-constant envelope for the signal, except for the cases where $|w_{11}| = |w_{12}| = ... = |w_{1N_{\text{sc}}}|$. For a defined pilot signal generation power share $\eta_1 \leq 1$, the set of possible solutions for the legacy scenario are as follows:

$$\mathcal{W}_1(\eta_1) = \left\{ \boldsymbol{w}_1 \in \mathbb{R}^{N_{\text{sc}} \times 1} \,\middle|\, \sqrt{w_{11}^2 + w_{12}^2 + ... + w_{1N_{\text{sc}}}^2} \leq \sqrt{\eta_1 N_{\text{sc}}} \right\} \tag{10}$$

This set describes an N_{sc}-dimensional sphere with radius $\sqrt{\eta_1 N_{\text{sc}}}$, with the center at the origin.

2.2.2 | *Optimistic Scenario: Constant-Envelope Signal With the MCS Data Waveform*

Another approach is to optimize the MCS of the pilot and choose an MCS for the data waveform such that the composite signal always has a constant envelope. This case can be considered as constant-envelope multiplexing (CEM), where the data waveform is a secondary user signal, but also acts as the IM component for the non-constant-envelope pilot waveform. In this optimistic scenario, the constellation points must reside on a circle with radius P and the center in the origin of the complex plane. Thus, we have the following:

$$1 \overset{!}{=} w_{1n}^2 + w_{2n}^2 \quad \forall n \in \mathcal{N} \tag{11a}$$

$$\Rightarrow \quad w_{2n} = \pm\sqrt{1 - w_{1n}^2} \quad \forall n \in \mathcal{N} \tag{11b}$$

$$\Rightarrow \quad -1 \le w_{1n} \le +1 \qquad \forall n \in \mathcal{N} \tag{11c}$$

which restricts the solution space of possible MCS weights. Choosing a weight w_{1n} for the pilot waveform for the n-th subchip essentially determines the amplitude of the weight w_{2n} of the data waveform, but leaves choices for the polarity. For simplicity, the weight w_{2n} of the data waveform in each n-th subchip is fixed to $\sqrt{1 - w_{1n}^2}$, setting the polarity to always be +1. The set of possible constant-envelope solutions for the optimistic scenario is the intersection of $\mathcal{W}_1(\eta_1)$ with an N_{sc}-dimensional cube with an edge length of 2 and the center at the origin:

$$\mathcal{W}_2(\eta_1) = \mathcal{W}_1(\eta_1) \bigcap \left[-1, +1\right]^{N_{sc} \times 1} \tag{12}$$

2.3 | Distortion and User Constraints

Incorporating realistic payload and receiver distortions into the navigation signal design process is key to finding optimal solutions that perform best given the imperfect transmitter and receiver hardware. This paper models distortion with nonlinear and linear components in the system model. The respective component models are introduced below.

2.3.1 | Nonlinear Distortion

Typical processes modeled in a nonlinear fashion include digital distortion, quantization, and signal amplification. In this study, only signal amplification by an HPA is modeled. Other nonlinear phenomena such as digital distortion and quantization are beyond the scope of this work. Because there is no public information available on the HPA characteristics of any GNSS satellite, a generic, memoryless, phase-compensated Saleh model (Beck et al., 2022), resembling the characteristics of the HPA used by Rebeyrol et al. (2006), is applied. As stated by Rapp (1991), a memoryless amplification following the NSGU and FGUU in the passband can be expressed in baseband notation using input amplitude to output amplitude (AM/AM) and input amplitude to output phase (AM/PM) characteristics. In this study, the AM/AM and AM/PM characteristics are given as follows:

$$g\left(x(t)\right) = g_A\left(\left|x(t)\right|\right) e^{j\left(g_\Phi\left(\left|x(t)\right|\right) + \operatorname{atan2}\left(\operatorname{Im}\{x(t)\}, \operatorname{Re}\{x(t)\}\right)\right)} \tag{13a}$$

$$g_A\left(\left|x(t)\right|\right) = \frac{p_1 \left|x(t)\right|}{1 + p_2 \left|x(t)\right|^2} \tag{13b}$$

$$g_\Phi\left(\left|x(t)\right|\right) = \frac{p_3 \left|x(t)\right|^2}{1 + p_4 \left|x(t)\right|^2} + p_5 \tag{13c}$$

These characteristics are defined by the five parameters $p_1 = 94.897$ (small-signal gain), $p_2 = 50.402$ W^{-2} ($= 1/x_0^2$, where x_0 denotes the input saturation amplitude), $p_3 = 24.715$ W^{-2}, $p_4 = 94.406$ W^{-2}, and $p_5 = -0.127$. These parameters were derived by solving for the Saleh characteristic such that the HPA model has a small-signal gain of 39.5 dB and such that a constant-envelope

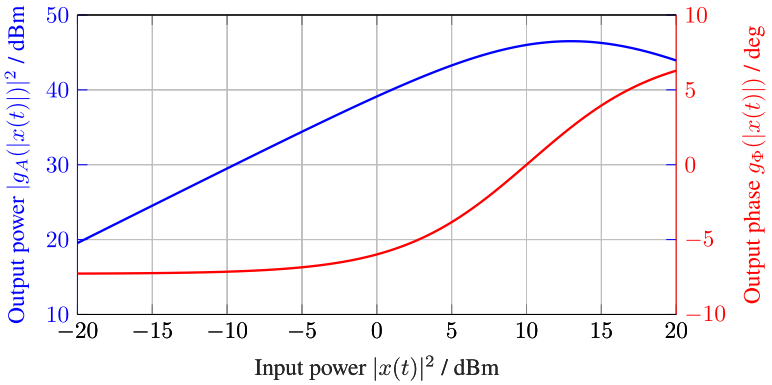

FIGURE 1 AM/AM and AM/PM characteristics of the memoryless HPA model

input signal $x(t)$ with a power of 10.0 dBm (= 0.01 W) has an output power of 46.0 dBm (≈39.8 W) with an input power backoff (IBO) of 3.0 dB and an output power backoff (OBO) of 0.5 dB. Figure 1 shows AM/AM and AM/PM functions for the HPA model used. With an average input power of 10 dBm and the resulting IBO and OBO, the HPA operates in the upper end of the transition region between the linear and saturation region. In this operating region, amplitude compression is already significant, resulting in correlation losses of non-constant-envelope inputs at the receiver due to mismatched replicas, as shown by Enneking et al. (2022).

2.3.2 | *Linear Distortion*

Filtering and path loss are typical processes that are modeled linearly. For the IMUX filter $h_{\mathrm{I}}(t)$, which models the band-limited behavior of digital-to-analog converter (DAC) results in a slightly non-constant input to the subsequent HPA, a phase-compensated sixth-order Butterworth characteristic with a two-sided 3-dB bandwidth of 204.60 MHz is assumed, inspired by the work presented by Rebeyrol (2007) in the context of GAL signal selection and optimization. We model the IMUX filter as identical for each payload characteristic, given the absence of publicly available data. However, a notable discrepancy in the behavior of DACs between satellite payloads due to aging and environmental effects is likely and may merit further investigation for fine-tuned distortion-aware signal designs, which is beyond the scope of this work. The OMUX filters $h_{\mathrm{O}}^{(k)}(t)$ are modeled based on linear payload characterizations of nine GPS IIF satellites in the L5 band with NORAD IDs 36585, 37753, 38833, 39166, 39533, 39741, 40105, 40294, and 40534 (Thölert et al., 2019). Figure 2 shows the absolute step responses, where $u(t)$ denotes the unit step function. Accounting for free space loss and transmitter and receiver antenna gains, we assume that $\gamma_{\mathrm{PL}} = -170.0$ dB for the path loss constant. The receiver front-end characteristic $h_{\mathrm{R}}^{(k)}(t)$ is implemented as a brick-wall filter with a two-sided bandwidth of 40.92 MHz. Consequently, the number of CPRCs is $K = 9$.

3 | PERFORMANCE MEASURES

The two selected performance measures assess the differential range bias and the average TOA estimation error SD over the distortion set $\mathcal{K}$. Each performance measure is derived from K metrics derived from K CPRCs. Because these two

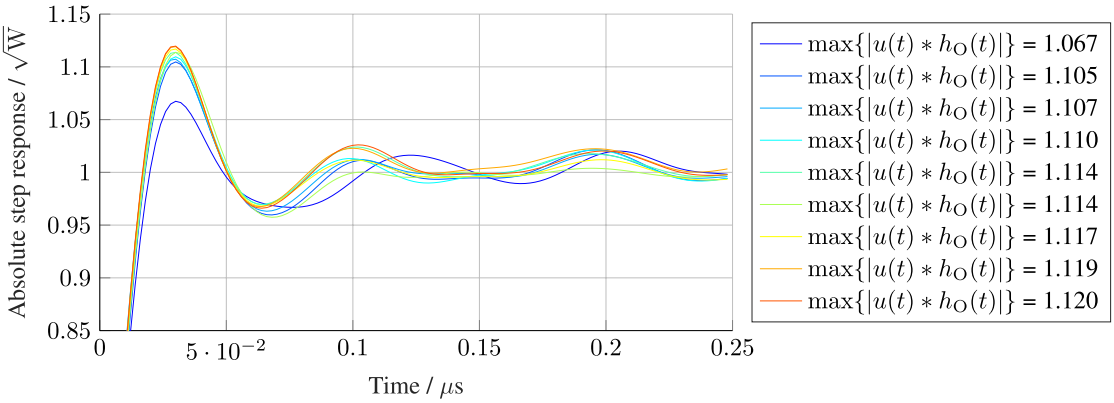

FIGURE 2 Step responses of linear payload characterizations of selected GPS IIF satellites

performance measures constitute the objective of the OP later on, the mathematical basis is described below.

3.1 | Range Bias Realization

To evaluate the differential range bias across the distortion set $\mathcal{K}$, it is necessary to assess the range bias for each distortion realization. Assuming a coherent early-late processing (CELP) scheme with an early, prompt, and late correlator, the range bias of the k-th realization is derived from the discriminators:

$$0 \stackrel{!}{=} \text{Re}\left\{R_{xc_1}\left(\hat{\tau}_x + \Delta/2\right)e^{j\hat{\varphi}_x}\right\} - \text{Re}\left\{R_{xc_1}\left(\hat{\tau}_x - \Delta/2\right)e^{j\hat{\varphi}_x}\right\} \tag{14a}$$

$$0 \stackrel{!}{=} \text{Re}\left\{R_{sc_1}^{(k)}\left(\hat{\tau}_s^{(k)} + \Delta/2\right)e^{j\hat{\varphi}_s^{(k)}}\right\} - \text{Re}\left\{R_{sc_1}^{(k)}\left(\hat{\tau}_s^{(k)} - \Delta/2\right)e^{j\hat{\varphi}_s^{(k)}}\right\} \quad \forall k \in \mathcal{K} \tag{14b}$$

where $\stackrel{!}{=}$ indicates "required to equal," Δ denotes the early-late correlator spacing, $\hat{\tau}_x$ is the TOA estimate of the pilot waveform of the composite transmit signal $x(t)$ before being subject to linear and nonlinear distortions, $\hat{\tau}_s^{(k)}$ denotes the TOA estimate of the pilot waveform of the satellite contribution $s^{(k)}(t)$ after filtering on the receiver side, $\hat{\varphi}_x$ is the estimate of the prompt correlator's phase of the pilot waveform of the composite transmit signal $x(t)$, and $\hat{\varphi}_s^{(k)}$ represents the estimate of the prompt correlator's phase of the pilot waveform of the satellite contribution $s^{(k)}(t)$. The following expressions:

$$R_{xc_1}(\tau) = \frac{1}{\sqrt{\eta_1 E_x}} \int_{t_0}^{t_0+T} x(t)\tilde{c}_1^*(t-\tau)\,\text{d}t \tag{15a}$$

$$R_{sc_1}^{(k)}(\tau) = \frac{1}{\sqrt{\zeta_1^{(k)} E_s^{(k)}}} \int_{t_0}^{t_0+T} s^{(k)}(t)\tilde{c}_1^*(t-\tau)\,\text{d}t \quad \forall k \in \mathcal{K} \tag{15b}$$

denote the cross-correlation functions (CCFs) of the composite transmit and satellite contribution signal with an energy-normalized and chip-shape-matched pilot replica $\tilde{c}_1(t) = c_1(t)/\sqrt{\eta_1 T}$ for the integration time T such that the auto-correlation function (ACF):

$$R_{c_1c_1}(\tau) = \int_{t_0}^{t_0+T} \tilde{c}_1(t)\tilde{c}_1^*(t-\tau)\mathrm{d}t \tag{16}$$

attains $R_{c_1c_1}(0) = \int_{t_0}^{t_0+T} |\tilde{c}_1(t)|^2 \, \mathrm{d}t = 1$. The CCFs are energy-normalized with the energy of the composite transmit signal $E_x = \int_{t_0}^{t_0+T} |x(t)|^2 \, \mathrm{d}t$, the energy of the satellite contribution in the receive signal $E_s^{(k)} = \int_{t_0}^{t_0+T} |s^{(k)}(t)|^2 \, \mathrm{d}t$, and the pilot reception energy coefficient:

$$\zeta_1^{(k)} = \frac{\left(\max_\tau \left\{\left|\int_{t_0}^{t_0+T} s^{(k)}(t)\tilde{c}_1^*(t-\tau)\mathrm{d}t\right|\right\}\right)^2}{\left(\max_\tau \left\{\left|\int_{t_0}^{t_0+T} s^{(k)}(t)\tilde{c}_1^*(t-\tau)\mathrm{d}t\right|\right\}\right)^2 + \left(\max_\tau \left\{\left|\int_{t_0}^{t_0+T} s^{(k)}(t)\tilde{c}_2^*(t-\tau)\mathrm{d}t\right|\right\}\right)^2} \tag{17}$$

which is a correlation-based estimate of the energy portion of the pilot waveform within the receive signal energy with $\tilde{c}_2(t) = c_2(t)/\sqrt{\eta_2 T}$, assuming that the pilot and data waveforms are uncorrelated. For instances in which the pilot waveform is designed to disperse a greater quantity of signal energy beyond the reception bandwidth than the data signal, the pilot reception energy coefficient will be less than the power share during signal generation. The range bias is determined by the result of the discriminator expressions in Equations (14a) and (14b). For one element in the distortion set k, the range bias amounts to the following:

$$\varepsilon^{(k)} = \hat{\tau}_s^{(k)} - \left(\hat{\tau}_x + \tau_0^{(k)}\right) = \hat{\tau}_s^{(k)} - \hat{\tau}_x - \tau_0^{(k)} \tag{18}$$

with $\tau_0^{(k)}$ denoting the signal propagation delay.

3.2 | Tracking Jitter Realization

The unsmoothed code tracking error jitter or the TOA estimation error SD of the unsmoothed code-phase assesses the ranging accuracy around a biased pseudorange measurement. A common metric for assessing this term in a distortion-free scenario would be the Gabor or RMS bandwidth, which would be a meaningful choice for the distortion-free composite satellite transmit signal $x(t)$, as used by Zhang et al. (2011a). Because this study aims to assess the impact of distortion and to optimize the pilot signal alone, an alternative expression for the code-phase TOA estimation error SD based on CCF properties is used, as introduced by Vergara et al. (2019). Consequently, the CELP TOA estimation error SD of the k-th realization may be expressed as follows:

$$\sigma^{(k)} = \sqrt{\frac{N_0}{4\zeta_1^{(k)} E_s^{(k)}} \frac{1 - R_{c_1c_1}(\Delta)}{\left(\mathrm{Re}\left\{\frac{\mathrm{d}}{\mathrm{d}t} R_{sc_1}^{(k)}\left(\Delta/2 - \tau_s^{(k)}\right)\right\}\right)^2}} \tag{19}$$

for a fixed early-late correlator spacing Δ and a noise density N_0, similar to previous work by Beck et al. (2022). The drawback of this expression is the dependence on a fixed early-late correlator spacing Δ. The advantage of this expression is that the tracking error jitter of one signal component can be isolated from the composite satellite contribution signal $s(t)$ and that the impact of distortions, which is reflected by a receiver power loss and CCF deformation, is assessed.

3.3 | Definition of Performance Measures

The K samples for the range bias and TOA estimation error SD yield the performance measures:

$$J_1 \triangleq c_0 \sqrt{\frac{1}{K}\sum_{k=1}^{K}\left(\varepsilon^{(k)} - \frac{1}{K}\sum_{k'=1}^{K}\varepsilon^{(k')}\right)^2} \quad \text{(SD of range biases)} \tag{20a}$$

$$J_2 \triangleq c_0 \frac{1}{K}\sum_{k=1}^{K}\sigma^{(k)} \quad \text{(mean of TOA estimation error SDs)} \tag{20b}$$

where c_0 denotes the speed of light. The first performance measure, J_1, is the SD of the range biases and indicates the impact of differential range biases on the end user. The second performance measure, J_2, evaluates the average unsmoothed code-phase TOA estimation error SD, which is also referred to as the mean tracking jitter later on. The performance measures J_1 and J_2 are the two metrics constituting the objective of the OP, as described hereafter.

4 | OPTIMIZATION PROBLEM

This section introduces the statement of the bi-objective OP and its reformulation.

4.1 | Problem Statement

The bi-objective OP is defined as follows:

$$\min_{\boldsymbol{w}_1 \in \mathbb{R}^{N_{\mathrm{sc}}}} \quad \alpha J_1 + (1-\alpha) J_2 \qquad \text{(objective)} \tag{21a}$$

$$\text{s.t.} \quad \eta_1 \le \eta_1^{\max} \qquad \text{(maximum pilot power share)} \tag{21b}$$

$$\varrho_{11} \le \varrho_1^{\max} \qquad \text{(maximum pilot LSPMPAR)} \tag{21c}$$

$$\mathrm{SSC}_{(1,q)} \le \mathrm{SSC}^{\max} \quad \forall q \in \mathcal{Q} \qquad \text{(maximum SSC)} \tag{21d}$$

$$|w_{1n}| \ge w_1^{\min} \quad \forall n \in \mathcal{N} \qquad \text{(minimum pilot weight amplitude)} \tag{21e}$$

$$|w_{2n}| \ge w_2^{\min} \quad \forall n \in \mathcal{N} \qquad \text{(minimum data weight amplitude)} \tag{21f}$$

$$J_1 \le J_1^{\max} \qquad \text{(maximum differential range bias)} \tag{21g}$$

$$J_2 \le J_2^{\max} \qquad \text{(maximum mean tracking jitter)} \tag{21h}$$

$$|w_{1n}| \le w_1^{\max} \quad \forall n \in \mathcal{N} \qquad \text{(maximum weight amplitude)} \tag{21i}$$

This problem minimizes the SD of the range biases and the mean of the TOA estimation error SDs of the pilot ranging signal over all K distortion realizations with the objective weight $\alpha \in [0,1]$ and the variable $\boldsymbol{w}_1$ (i.e., the pilot weight vector). Setting $\alpha = 1$ results in a pure differential bias optimization. Setting $\alpha = 0$ results in a pure mean tracking jitter optimization. This comprehensive OP is subject to

a number of constraints, the purpose of which is to ensure not only applicability, but also favorable pilot signal properties. The first constraint in Equation (21b) provides an upper bound for the power share of the pilot waveform η_1 and acts only as an average power constraint for the pilot waveform. Equation (21c) constrains the largest side peak to main peak amplitude ratio (LSPMPAR), which is relevant in the context of robustness to multipath propagation. Considering noncoherent early-late processing (NELP), the LSPMPAR $\varrho_{11} = \max\{|\upsilon_{1n'}| / \upsilon_{10'} \mid n' \in \mathcal{P}\}$ is defined as the ratio of the secondary stable-tracking side-peak with the largest amplitude to the amplitude of the main peak in the ACF of the pilot MCS, which is reflected by the NELP peak index set $\mathcal{P} := \{n' \mid \upsilon_{1(n'-1)} < \upsilon_{1n'} > \upsilon_{1(n'+1)} \vee \upsilon_{1(n'-1)} > \upsilon_{1n'} < \upsilon_{1(n'+1)}\}$. Details regarding the derivation of the ACF of an MCS with any given weight vector are presented in Appendix A. The constraint in Equation (21d) uses the spectral separation coefficient (SSC) measure to reflect the requirements with respect to MAI in already occupied bands, such as the lower and upper L-band, to yield an optimized MCS waveform that does not adversely affect existing services. This study uses the following expression:

$$\mathrm{SSC}_{(1,q)} = \frac{\int_{-B/2}^{+B/2} G_1(f) G_q(f) \mathrm{d}f}{\int_{-\infty}^{+\infty} G_1(f) \mathrm{d}f \int_{-\infty}^{+\infty} G_q(f) \mathrm{d}f} \tag{22}$$

as, for instance, defined by Betz (2015) for a two-sided front-end bandwidth B with units of 1/Hz, where $G_1(f)$ denotes the power spectral density (PSD) of the MCS pilot waveform and $G_q(f)$ denotes the PSD of another waveform using an index $q \in \mathcal{Q}$ for indicating waveform pairs for which the SSC shall not be exceeded. Details regarding the derivation of the PSD of an MCS are presented in Appendix B. Equations (21e) and (21f) aim to restrict solutions with subchip weights close to 0 to avoid receiver dynamic issues. Equations (21g) and (21h) limit the SD of the range biases and the mean of the TOA estimation error SDs. These constraints are, to some extent, also reflected in the objective, but they are incorporated in the constraint set to ensure suitable solutions for a pure differential bias or tracking error jitter optimization. The constraint in Equation (21i) is only relevant for the constant-envelope approach in the optimistic scenario and limits the value space of each weight w_{1n}, such that a real-valued w_{2n} exists for every $n \in \mathcal{N}$.

4.2 | Problem Reformulation

The OP is a nonlinear and nonconvex programming problem. One method for handling the constraints is the introduction of penalty functions with corresponding penalty coefficients (Nocedal & Wright, 2006). The problem can then be stated as follows:

$$\begin{aligned} \min_{\boldsymbol{w} \in \mathbb{R}^{N_{\mathrm{sc}}}} \; & \tilde{\alpha} \tilde{J}_1 + (1 - \tilde{\alpha}) \tilde{J}_2 + \mu_1 \left[\eta_1 - \eta_1^{\max} \right]_+^2 + \mu_2 \left[\varrho_{11} - \varrho_1^{\max} \right]_+^2 \\ & + \mu_3 \sum_{q=1}^{Q} \left[\mathrm{SSC}_{(1,q)} - \mathrm{SSC}^{\max} \right]_+^2 + \mu_4 \sum_{n=1}^{N_{\mathrm{sc}}} \left[w_1^{\min} - |w_{1n}| \right]_+^2 + \mu_5 \sum_{n=1}^{N_{\mathrm{sc}}} \left[w_2^{\min} - |w_{2n}| \right]_+^2 \\ & + \mu_6 \left[J_1 - J_1^{\max} \right]_+^2 + \mu_7 \left[J_2 - J_2^{\max} \right]_+^2 \end{aligned} \tag{23}$$

where $[z]_+^2 = (\max\{0,z\})^2$ denotes an l^2-merit function, $\tilde{J}_1$ is the normalized objective J_1, $\tilde{J}_2$ represents the normalized objective J_2, and $\mu_1,...,\mu_7 \in \mathbb{R}_+$ denotes the real-valued non-negative penalty function coefficients. Normalizing the objective functions into the domain of [0,1] was imperative for deriving meaningful trade-off solutions in the numerical implementation. This objective was accomplished by systematically adjusting the parameter α. In the absence of adequate scaling, the magnitudes of the objective values can become imbalanced, resulting in biased solutions and skewing of the intended trade-off. In ensuring a balanced optimization process, it was necessary to normalize the objectives prior to the application of the bi-objective optimization framework. A thorough examination of the normalization process in the context of multi-objective optimization has been reported by Miettinen (1998). The value space constraint may be implemented in such a way that a solver must not leave $\mathcal{W}_1'(\eta_1)$ or $\mathcal{W}_2'(\eta_1)$, respectively. One approach for finding sufficient local minima is an initial brute-force search on the convex hull of $\mathcal{W}_1'(\eta_1)$ or $\mathcal{W}_2'(\eta_1)$ to find suitable start vectors for a subsequent search with the downhill simplex method.

4.3 | Trade-Offs Along Pareto Curves

As a result of the optimization of the bi-objective OP with a varying objective weight α, a swarm of solutions can be found that form a Pareto curve defined by a finite set of solutions, each found for an individual objective weight α. Each solution along the Pareto curve represents a potential optimal candidate, contingent upon the specific trade-off criteria. One straightforward approach for selecting a signal candidate is to inspect the performance enhancement relative to a chosen performance, which serves as a reference point. We use the following two performance change parameters:

$$\chi_{1,m} = J_{1,m}^*/J_1^{\text{ref}} - 1 \qquad \forall m \in \mathcal{M} \tag{24a}$$

$$\chi_{2,m} = J_{2,m}^*/J_2^{\text{ref}} - 1 \qquad \forall m \in \mathcal{M} \tag{24b}$$

to assess the change in joint ranging performance of the m-th optimal solution point $\left(J_{1,m}^*, J_{2,m}^*\right)$ on the Pareto curve with respect to the reference performance point $\left(J_1^{\text{ref}}, J_2^{\text{ref}}\right)$, where each Pareto curve consists of M optimal solutions defining the index set $\mathcal{M} = \{1,...,M\}$. If $\chi_{1,m} < 0$ or $\chi_{2,m} < 0$, the differential range bias or tracking jitter is reduced, respectively. In this study, the reference point $\left(J_1^{\text{ref}}, J_2^{\text{ref}}\right)$ is characterized by the transmission of two BPSK-R(10) waveforms in I and Q, representing the current status quo of GPS L5. Using the two performance change parameters $\chi_{1,m}$ and $\chi_{2,m}$ defined by Equations (24a) and (24b), a multitude of trade-off strategies might be used to achieve a meaningful trade-off, including the following strategies:

$$\arg\min \chi_{1,m} \qquad \forall m \in \{m \in \mathcal{M} \,|\, \chi_{2,m} \le 0\} \quad \text{(Trade-off 1)} \tag{25a}$$

$$\arg\min \chi_{2,m} \qquad \forall m \in \{m \in \mathcal{M} \,|\, \chi_{1,m} \le 0\} \quad \text{(Trade-off 2)} \tag{25b}$$

$$\arg\min \chi_{1,m} + \chi_{2,m} \qquad \forall m \in \mathcal{M} \quad \text{(Trade-off 3)} \tag{25c}$$

$$\arg\min \chi_{1,m}\chi_{2,m} \qquad \forall m \in \mathcal{M} \quad \text{(Trade-off 4)} \tag{25d}$$

Trade-off 1 in Equation (25a) aims to minimize the SD of the range biases while not increasing the mean of the TOA estimation error SDs. In contrast, trade-off 2 in Equation (25b) aims to minimize the mean of TOA estimation error SDs while not increasing the SD of the range biases. The goal of the latter rationales, expressed by Equations (25c) and (25d), is to minimize the sum and product of the change parameters, respectively.

5 | NUMERICAL RESULTS

This section presents the results of the optimization of the defined OP for specific simulation parameters. First, the simulation parameters are presented, and then, insights into the structure of the investigated solutions are provided. Finally, this section illustrates the set of possible solutions by varying the objective weight α, forming Pareto curves for each scenario and imposed MCS symmetry constraint. Additionally, the characteristics of four selected MCSs are presented for each scenario.

5.1 | Simulation Parameters

This study examines the optimization of an MCS for a pilot waveform in two distinct scenarios. The first scenario entails a reshaping of the pilot waveform's chip shape, while the data waveform's chip shape remains unaltered. The second scenario involves a reshaping of the pilot and data waveform's chip shape, with the objective of optimizing the ranging performance of the pilot while maintaining a constant envelope for the complex signal. The selection of these scenarios is intended to illustrate the range of potential performance improvements that can be achieved. The respective simulation parameters of the defined scenarios are provided in Table 1, where $f_b = 1/T_b = 1.023$ MHz denotes the base frequency relevant to GNSS. In both scenarios, the noise density is set to $N_0 = -204$ dBW/Hz, resulting in a carrier-to-noise density ratio (C/N_0) in the range of 42 to 43 dB-Hz for the composite signal. The early-late correlator spacing is set to $\Delta = T_b / 20 \approx 48.88$ ns. The primary range codes for pilot and data components of currently deployed GPS L5 payloads were used for the range codes in this simulation. Furthermore, $\eta_1^{\max} = 0.5$, $\varrho_1^{\max} = 0.5$, $\mathrm{SSC}^{\max} = -71.86$ dB/Hz (i.e., self-SSC of BPSK-R(10)), $w_1^{\min} = 0.1$, $w_2^{\min} = 0.1$, $c_0 J_1^{\max} = 10.0$ m, and $c_0 J_2^{\max} = 10.0$ m. The SSCs relevant to the SSC constraint are the pilot MCS self-SSC, the data/pilot MCS SSC, and the SSC of the pilot MCS and BPSK-R(10). The penalty function coefficients were selected in a manner that ensured that the magnitude of the corresponding penalty function

TABLE 1
Parameters of Signal Generation Scenarios

	Legacy scenario		Optimistic scenario	
Channel	pilot	data	pilot	data
CEM	no		yes	
Pulse shape	MCS	rectangular	MCS	MCS
f_c / f_b	10	10	10	10
N_{sc}	10	-	10	10
N_{code}	10230	10230	10230	10230

was comparable to that of the objective function. The penalty function coefficients were set to $\mu_3 = 1$, $\mu_1 = 10^2$, $\mu_6 = \mu_7 = 10^3$, and $\mu_2 = \mu_4 = \mu_5 = 10^4$.

5.2 | Restriction to a Symmetric MCS

To apply a heuristic approach for finding suitable start vectors by evaluating the nonconvex OP, a dimensionality reduction is key for handling the complexity involved. A trivial way to reduce the dimension of the OP from N_{sc} to $N_{\mathrm{sc}}/2$ is to consider only MCSs of a special structure. This work considers waveforms with even N_{sc} and that are, with respect to the pulse center, axially symmetric (A-sym) or point symmetric (P-sym) MCSs. Consequently, only MCSs with the following weight relationships for the pilot waveform were considered in this investigation:

$$\text{A-sym:} \quad w_{ln} = +w_{l(N_{\mathrm{sc}}-n+1)} \qquad \forall (l,n) \in \mathcal{L} \times \mathcal{N} \tag{26a}$$

$$\text{P-sym:} \quad w_{ln} = -w_{l(N_{\mathrm{sc}}-n+1)} \qquad \forall (l,n) \in \mathcal{L} \times \mathcal{N} \tag{26b}$$

The symmetry constraint is inspired by the structure of a majority of navigation signals currently broadcast by GNSS, but it is also imposed to effectively reduce the computational complexity of the OP. However, the introduction of the symmetry assumption requires a case distinction for A-sym and P-sym MCS. Furthermore, distortion-aware nonsymmetric MCSs, which may perform better than symmetric MCSs, are excluded from the set of solutions and are therefore beyond the scope of this work.

5.3 | Pareto Curves

The Pareto curves for the bi-objective OP illustrate the set of optimal solutions for varying objective weights. The objective weight enables the formulation of a trade-off between the two opposing objectives of differential range bias and mean tracking jitter minimization. Figure 3 illustrates the performance of the found solutions of the optimization, given the chosen simulation parameters with a varying objective weight $\alpha \in [0,1]$ for each scenario and symmetry assumption. In addition to the Pareto curves, which are the result of a distortion-aware optimization, Figure 3 also depicts the current reference operating point, which employs a BPSK-R(10) pilot and data component with $c_0 J_1 = 6.59$ cm and $c_0 J_2 = 1.26$ m.

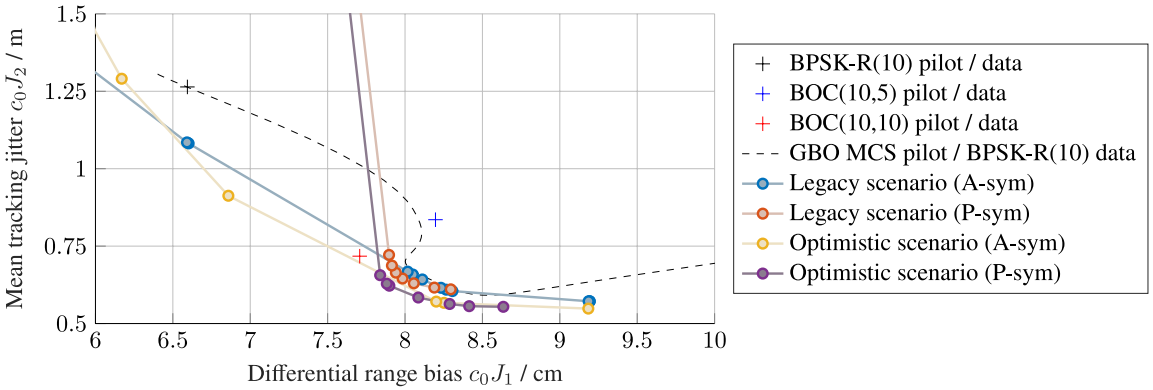

FIGURE 3 Pareto curves for $N_{\mathrm{sc}} = 10$

In addition, the performance of BOC(10,5) ($c_0J_1 = 8.20$ cm, $c_0J_2 = 0.84$ m) and BOC(10,10) ($c_0J_1 = 7.71$ cm, $c_0J_2 = 0.72$ m) signals is shown, which exhibit a lower mean tracking error jitter but experience an increased differential bias compared with the BPSK-R(10) signal. Furthermore, the performance of a Gabor bandwidth-optimized (GBO) MCS is also presented for a fair comparison. The optimization strategy for deriving the GBO MCS uses as an input the PSD of the pulse basis functions, whose exact shape are dependent on T_c and N_{sc}, and a target two-sided front-end bandwidth. Details on finding a GBO MCS for those parameters are briefly provided in Appendix C based on the work of Zhang et al. (2011a). The performance of the GBO MCS is shown in Figure 3 for a fixed $T_c = T_b/10$ and $N_{sc} = 10$, but varying target front-end bandwidths. In this study, the GBO MCS with minimal mean tracking jitter is optimized for a front-end bandwidth of 27.621 MHz ($c_0J_1 = 8.54$ cm, $c_0J_2 = 0.59$ m). GBO MCSs that are optimized for a front-end bandwidth of 23.529 MHz ($c_0J_1 = 8.26$ cm, $c_0J_2 = 0.62$ m) or higher violate the LSPMPAR constraint $\varrho_1^{\max} = 0.5$. Based on the solutions along the Pareto curves with respect to the GPS L5 performance and the performance of the GBO MCS, multiple observations can be made that are specific to this example:

1. Distortion-aware optimized A-sym MCSs can achieve a simultaneous reduction in differential range bias or mean tracking jitter with respect to the reference operating point.
2. Distortion-aware optimized P-sym MCSs effectively reduce mean tracking jitter, but systematically increase the differential range bias with respect to the reference operating point.
3. In the majority of instances, the optimistic scenario demonstrates superior performance in comparison to its legacy counterpart for the same symmetry constraint imposed on the MCS.
4. In a setup that accounts for distortions, the performance of the GBO MCS is worse than that of P-sym MCSs in the low-tracking-jitter region owing to a model mismatch and is also unable to reduce differential biases.

In light of these observations, it can be concluded that distortion-aware optimized MCSs are capable of achieving enhanced ranging performance in terms of differential range bias and mean tracking jitter in realistic scenarios when compared with the current status quo, as well as when compared with more wideband waveforms such as the BOC(10,5) and BOC(10,10) and even GBO MCSs. The advantage of this distortion-aware navigation signal design methodology is that it produces a set of optimal solutions from which a decision-maker can select the most suitable option. For instances in which it is challenging to monitor differential range biases, a decision-maker may select an MCS that minimizes these biases while maintaining tracking jitter performance in relation to a reference operating point. Conversely, for scenarios in which differential range biases are readily assessable and distributed to each user, a decision-maker may select an MCS that solely minimizes mean tracking jitter, relying on robust differential range bias monitoring and propagation to users. The primary limitation of this approach is that the set of solutions is finite and can only be augmented through an iterative search process. In the context of this case study, we identified MCSs that demonstrated the capacity to either reduce the differential range bias by 6.4% while simultaneously increasing the mean tracking jitter relative to the reference operating point by 2.1% or to reduce the mean tracking jitter by 56.2% while concurrently increasing the

differential range bias by 31.0% relative to the aforementioned reference operating point. A decision-maker must evaluate whether the performance improvements in terms of differential range bias or mean tracking error jitter reduction are sufficient to justify replacing rectangular waveforms with distortion-aware optimized MCS waveforms.

5.4 | Power Losses of Two-Component Signals Along the Signal Propagation Chain

The spectral occupation of an MCS waveform's PSD beyond the transmitter and receiver bandwidths is an inherent property of this type of waveform. Consequently, each MCS signal candidate will spill signal energy beyond the respective filter passbands, resulting in a loss of signal power. To illustrate the influence of the optimization weight α, the choice of signal generation scenario, and MCS symmetry on signal power loss, Figure 4 provides an illustration of the signal power after each step in signal formation. The HPA signal power loss is determined by the ratio of the IMUX-filtered and subsequently amplified complex HPA power output of a constant-envelope signal that possesses a mean signal power equivalent to that of the IMUX-filtered signal. As shown in Figure 4, it is evident that for all scenarios and MCS symmetries, the pure solution that exclusively minimizes the tracking jitter (i.e., $\alpha = 0$) leads to greater signal power losses compared with the solution where a combination of the differential range bias and tracking jitter (in the shown example, $\alpha = 0.97$) is minimized. A comparison of the legacy scenario with the optimistic signal generation scenario reveals that the former exhibits higher signal power at the receiver stage, yet experiences greater losses at the HPA due to the heightened non-constancy that arises from using the BPSK-R(10) as the data waveform. Conversely, in the optimistic scenario, although the solutions exhibit marginal losses induced by the HPA, they tend to experience a greater overall reduction in signal power.

5.5 | Characteristics of Selected Optimal MCSs

To further analyze elements of the Pareto curves shown above, this section presents the characteristics of selected distortion-aware optimized MCSs. In the

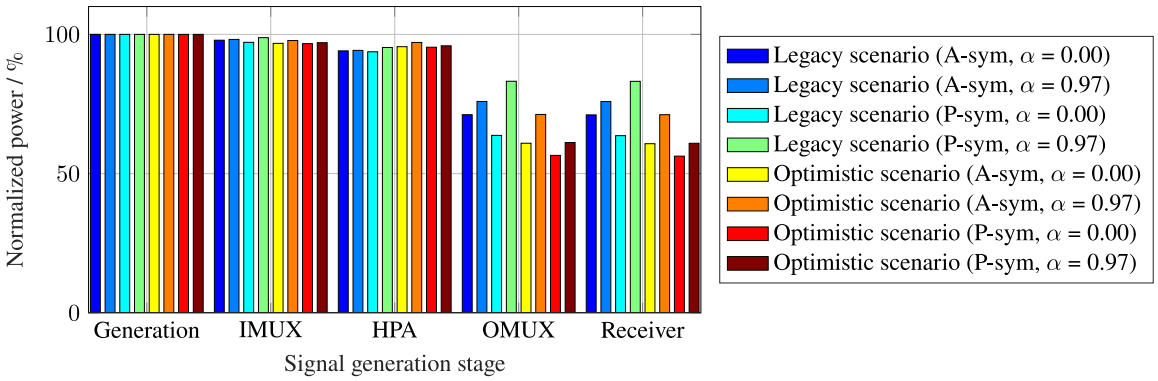

FIGURE 4 Cumulative signal power loss of two-component signal power for selected MCSs on the Pareto curve, with $N_{sc} = 10$

event that a decision-maker chooses to implement an optimized MCS, a number of trade-off rationales, as outlined in Equations (25a)–(25d), could be used to select an MCS for each scenario. The choice of these trade-off rationales is intended to show a sufficient range of distortion-aware optimized MCSs, but these options may be suboptimal for specific use cases.

5.5.1 | *Time Domain*

One domain meriting further investigation is the time domain of the optimized MCSs. Figures 5 and 6 illustrate the optimal MCSs in the time domain, which are elements of the Pareto curve selected according to the trade-off rationale for each scenario, where the notation MCS_p merely refers to use of the MCS for the pilot waveform. Correspondingly, the notation MCS_d, which will be used in the subsequent section, denotes the MCS of the data waveform. As illustrated in Figure 5, the MCS in the legacy scenario resulting from the first, second, and fourth trade-off rationales are A-sym. In contrast, the MCS resulting from the third trade-off rationale is P-sym. Although the maximum amplitude subchip weight constraint is inactive for the legacy scenario, no amplitude subchip weight greater than 1 is part of any solution. Figure 6 shows that the MCSs resulting from the first and second trade-off rationales are A-sym. In contrast, the MCSs resulting from the third and fourth trade-off rationales are P-sym.

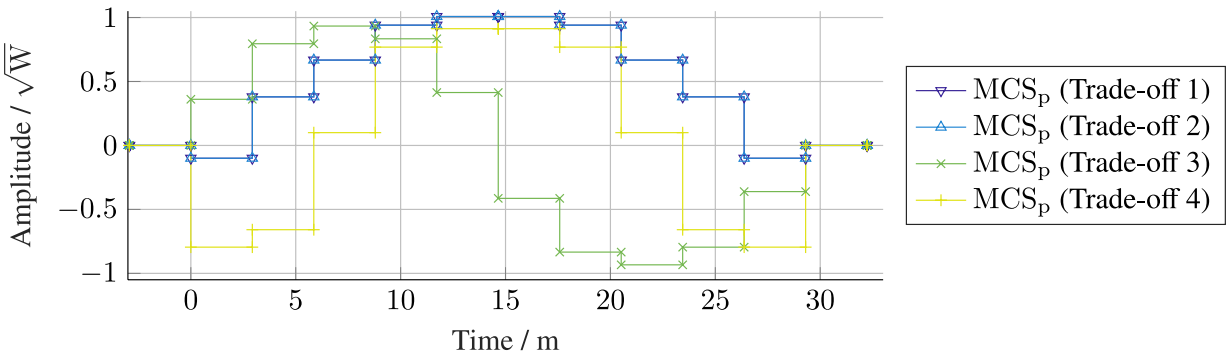

FIGURE 5 Selected optimal MCSs along the Pareto curve for the legacy scenario

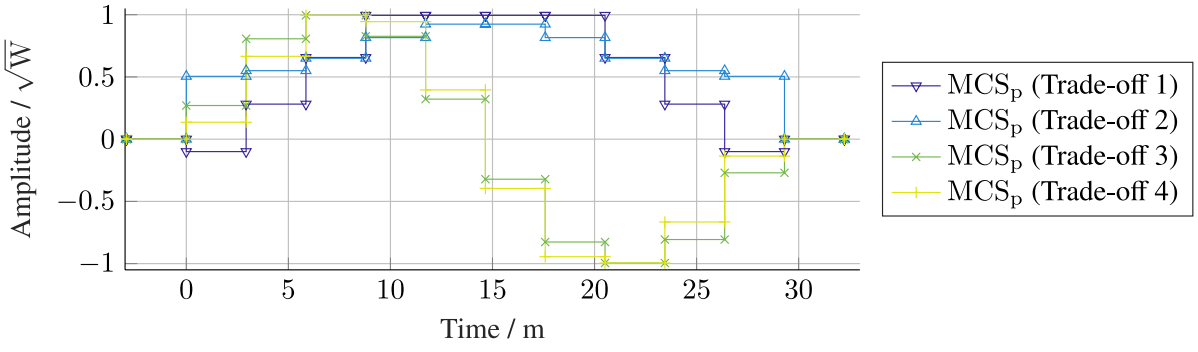

FIGURE 6 Selected optimal MCSs along the Pareto curve for the optimistic scenario

5.5.2 | Power Spectral Densities

As illustrated in Figures 7 and 8, the evaluation of the PSD of the selected MCSs indicates that the trade-offs that prioritize a reduction or disallow an increase in the differential range bias with respect to the reference operating point (i.e., trade-offs 1 and 2) result in the allocation of signal power to the center of the band. This power allocation is performed with the objective of preventing an accumulation of distortion at the band edges, where distortions are more prevalent. The main lobe of these MCSs is observed to have a width that is greater than that of the BPSK-R(10). The secondary side lobes exhibit a reduction in signal strength and (partially) extend beyond the target reception bandwidth of 40.92 MHz. Conversely, the trade-offs that prioritize the minimization of the mean tracking jitter over the differential range bias (i.e., trade-offs 3 and 4) allocate the signal power closer to the band edges of the payload and receiver front-end characteristics while accounting for distortions. The respective MCSs exhibit two primary main lobes, which contain the majority of the signal power. The incorporation of distortion into the signal design process enables more accurate model matching, thereby enabling distortion-aware MCSs to outperform purely GBO MCSs in realistic signal propagation settings.

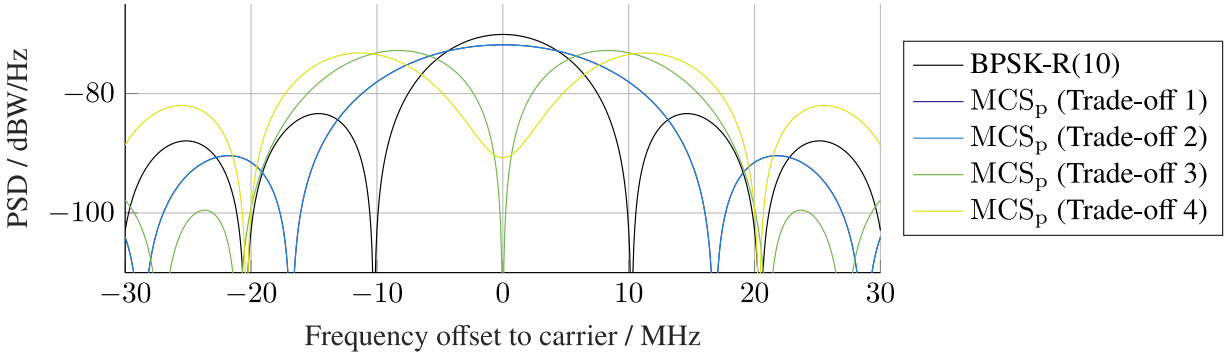

FIGURE 7 PSD of selected optimal MCSs along the Pareto curve for the legacy scenario

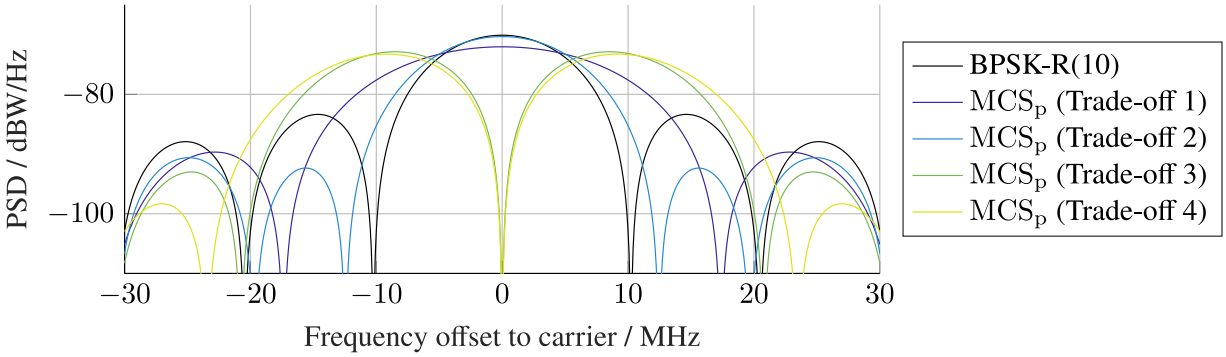

FIGURE 8 PSD of selected optimal MCSs along the Pareto curve for the optimistic scenario

5.5.3 | Spectral Separation

The trade-offs that favor mean tracking jitter reduction over differential range bias reduction spread their signal power closer to the edge of the band, maximizing their Gabor or RMS bandwidth to minimize mean tracking jitter. Tables 2 and 3 show that in both scenarios, all selected pilot MCSs have a lower self-SSC and SSCs with the data MCS and the legacy BPSK-R(10) than the BPSK-R(10) self-SSC of −71.86 dB/Hz. Furthermore, in both scenarios, the data/pilot SSC is lower than the current BPSK-R(10) self-SSC. Therefore, the application of an MCS to the pilot and possibly the data waveform may be an approach for mitigating upcoming MAI issues with the emerging LEO-PNT.

However, accurately defining a mission-specific SSC constraint for these types of scenarios requires additional system parameters. These parameters include satellite orbits, transmit antenna gain patterns, and signal placement within a specific frequency band. These parameters are necessary to compute a realistic upper bound for the SSC and to assess regulatory compliance in a mission-specific context. These parameters are particularly relevant in spectrally congested GNSS bands, such as the L1/E1 band. While a dedicated analysis in this area would be valuable, it is beyond the scope of this study.

5.5.4 | Auto-Correlation Functions

It is of interest to examine the shape of the ACFs of the selected MCSs, as illustrated in Figures 9 and 10. In the context of the presented case study, the application of trade-offs 1 and 2 results in the generation of MCSs with an ACF that exhibits a single main peak and no secondary side peaks. Employing these MCSs would

TABLE 2
SSCs in dB/Hz for the Legacy Scenario, With a Two-Sided Front-End Bandwidth of 40.92 MHz

Mapping	Trade-off 1	Trade-off 2	Trade-off 3	Trade-off 4
MCSp/MCSp	−73.30	−73.30	−74.28	−75.27
MCSp/MCSd	−72.85	−72.85	−78.16	−81.96
MCSd/MCSd	−71.86	−71.86	−71.86	−71.86
MCSp/BPSK–R(10)	−72.85	−72.85	−78.16	−81.96
MCSp/BPSK–R(1)	−71.92	−71.92	−88.16	−88.55
MCSd/BPSK–R(10)	−71.86	−71.86	−71.86	−71.86
MCSd/BPSK–R(1)	−70.25	−70.25	−70.25	−70.25

TABLE 3
SSCs in dB/Hz for the Optimistic Scenario, With a Two-Sided Front-End Bandwidth of 40.92 MHz

Mapping	Trade-off 1	Trade-off 2	Trade-off 3	Trade-off 4
MCSp/MCSp	−73.50	−71.84	−74.36	−74.77
MCSp/MCSd	−75.22	−72.42	−79.90	−81.13
MCSd/MCSd	−74.91	−72.74	−73.99	−74.64
MCSp/BPSK–R(10)	−73.00	−71.87	−78.35	−79.05
MCSp/BPSK–R(1)	−72.13	−70.46	−88.35	−89.05
MCSd/BPSK–R(10)	−74.02	−72.35	−72.94	−73.27
MCSd/BPSK–R(1)	−71.97	−70.55	−71.22	−71.45

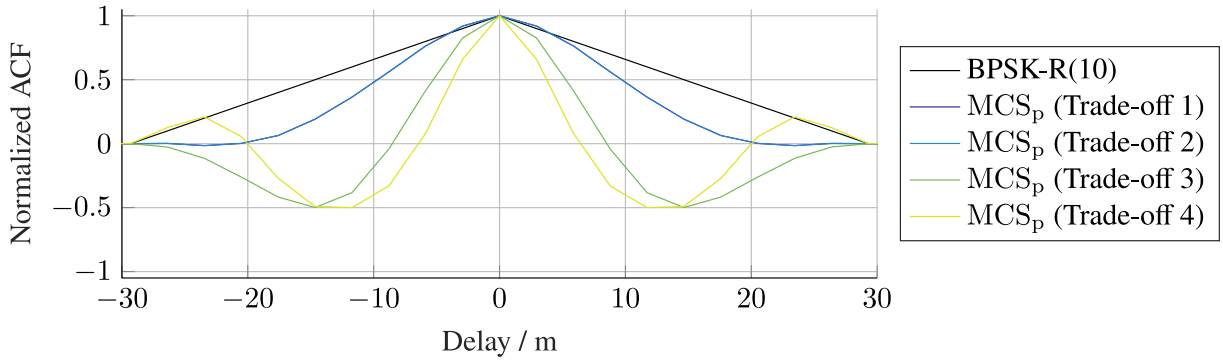

FIGURE 9 ACF of selected optimal MCSs along the Pareto curve for the legacy scenario

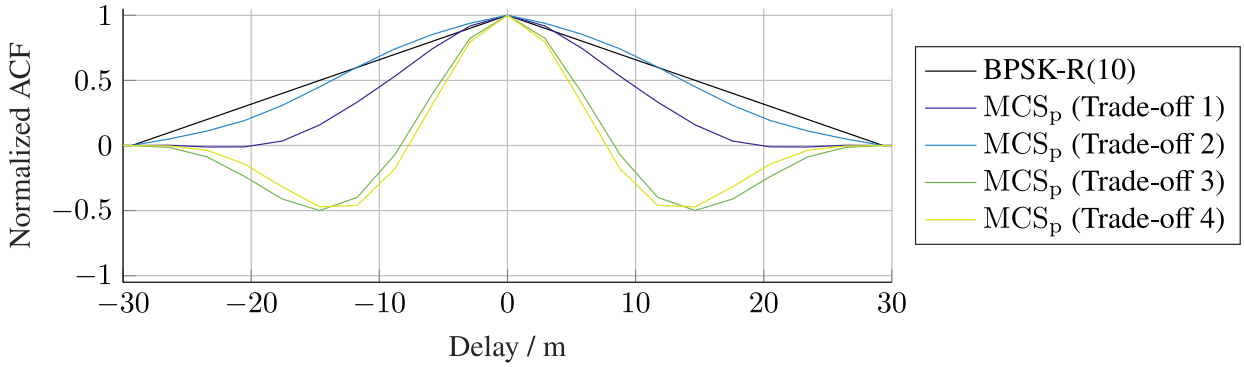

FIGURE 10 ACF of selected optimal MCSs along the Pareto curve for the optimistic scenario

allow for unambiguous tracking, similar to BPSK-R(10) signals. The application of trade-offs 3 and 4 results in the selection of MCSs with a main peak exhibiting a steeper slope than the BPSK-R(10) waveforms and, consequently, superior tracking performance. However, these MCSs also display secondary side peaks, necessitating the implementation of tracking methods capable of resolving code-phase ambiguity. The LSPMPAR constraint is relevant for the latter MCSs, which prevents the LSPMPAR from being larger than $\varrho_1^{\max} = 0.5$. It should be noted that the ACF of the GBO MCS may exhibit a main peak with a steeper slope, corresponding to a larger Gabor bandwidth, than that of the distortion-aware MCS. However, in the presence of distortions, the GBO MCS is susceptible to stronger correlation losses and stronger smoothing of the CCF, resulting in inferior performance compared with the distortion-aware MCS, as evidenced by Figure 3.

5.5.5 | *Multipath Error Envelopes*

An often-used metric for illustrating the range of errors induced by multipath propagation is the multipath ranging error envelope (MREE), which assumes a two-ray signal propagation with a line-of-sight (LOS) and a non-LOS (NLOS) path with a time delay, where the power of the NLOS path is attenuated by 3 dB compared with the LOS path. Figures 11 and 12 show the MREEs of the selected MCS for each scenario. The MREE were calculated by assuming a bandwidth of

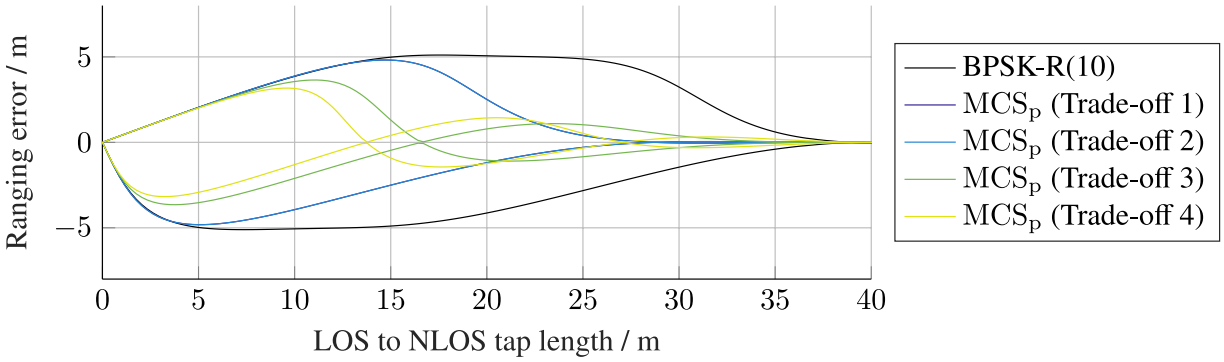

FIGURE 11 Multipath error envelopes for the legacy scenario

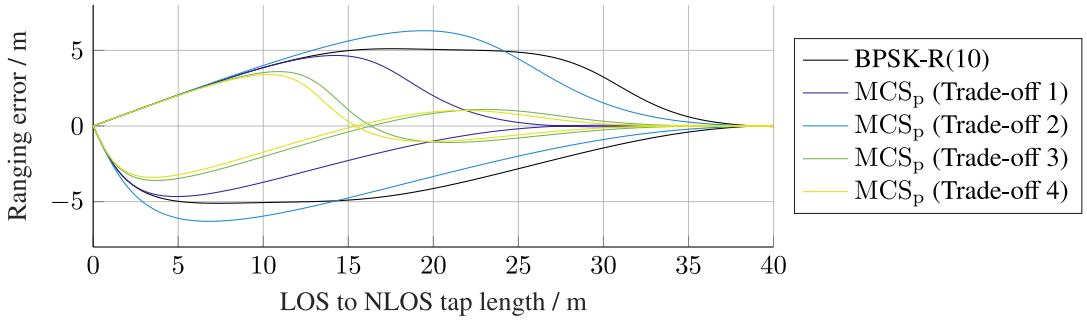

FIGURE 12 Multipath error envelopes for the optimistic scenario

40.92 MHz and an early-late spacing of $\Delta = T_b / 20$. The majority of the selected distortion-aware MCSs result in an earlier tapering and reduction of the MREE in comparison to the BPSK-R(10) MREE, indicating that they are more effective in suppressing errors induced by multipath propagation. The MREEs of low-tracking-jitter MCSs exhibit multiple humps that decrease in size rather than a single larger hump, which is a consequence of their steeper-sloped multi-peaked ACF. These findings suggest the potential for enhanced multipath robustness when utilizing distortion-aware MCSs.

6 | CONCLUSION

This study examined the potential advantages of distortion-aware MCS optimization, using the GPS L5 data/pilot waveforms as a case study. It can be concluded that although the use of MCSs instead of rectangular pulse shapes introduces an additional layer of complexity for the receiver architecture, for applications that require high accuracy and a high level of safety, the use of distortion-aware optimized MCSs can be highly beneficial in terms of mean tracking error jitter as well as in terms of reducing differential range bias. In this particular case study, the application of optimized MCSs resulted in a reduction of either the differential range bias up to 6.4% or the mean tracking jitter up to 56.2% with respect to the performance of the GPS L5 signal. The comprehensive OP introduced here considers a variety of relevant constraints, including multipath robustness and realistic distortion, as well as constraints imposed by the transmitter and receiver hardware.

Our findings demonstrate that the integration of distortion considerations into the signal optimization methodology facilitates the real-world applicability of distortion-aware MCSs, which outperform GBO MCSs in distortion-affected signal propagation environments. Moreover, this approach allows for the generation of optimal solutions along a Pareto curve, thereby enabling decision-makers to select the necessary trade-offs between the conflicting objectives of differential range bias and mean code-phase tracking error jitter reduction. It can be concluded that distortion-aware optimized MCSs are promising contenders for high-accuracy signals provided by LEO-PNT, PNT services for lunar exploration, and future generations of GNSSs, given the robust ranging performance increase and looming RFC issues in the L-band.

Further research could investigate the potential of distortion-aware nonsymmetric MCS optimization and waveform staggering. In addition, the performance of the secondary signal may be a valuable additional factor to consider in a joint optimization process with the primary signal, as well as the incorporation of performance-degrading effects such as digital distortion and realistic receiver front-end characteristics. A subsequent analysis is warranted to investigate the trade-off between band-limited CDMA chip shapes, such as PSWFs, and time-limited chip shapes, including MCSs.

ACKNOWLEDGMENTS

This work was carried out within the framework of the project HiGAIN at the German Aerospace Center (DLR).

CONFLICT OF INTEREST

The authors declare no conflicts of interest.

REFERENCES

Antreich, F., & Nossek, J. A. (2011). Optimum chip pulse shape design for timing synchronization. *2011 IEEE International Conference on Acoustics, Speech and Signal Processing (ICASSP)*, 3524–3527. https://doi.org/10.1109/ICASSP.2011.5946238

Antreich, F., Nossek, J. A., Issler, J.-L., & Meurer, M. (2009). Joint optimization of spectral separation and navigation performance in GNSS signal design. *Proc. of the 22nd International Technical Meeting of the Satellite Division of the Institute of Navigation (ION GNSS 2009)*, Savannah, GA, 2852–2859. https://www.ion.org/publications/abstract.cfm?articleID=8700

Ávila Rodríguez, J. Á. (2008). *On generalized signal waveforms for satellite navigation* [Doctoral dissertation, University der Bundeswehr Munchen]. https://athene-forschung.unibw.de/doc/86167/86167.pdf

Ávila Rodríguez, J. Á., Hein, G. W., Wallner S., Issler, J.-L., Ries, L., Lestarquit, L., de Latour, A., Godet, J., Bastide, F., Pratt, T., & Owen, J. (2007). The MBOC modulation: The final touch to the Galileo frequency and signal plan. *Proc. of the 20th international technical meeting of the satellite Division of the Institute of Navigation (ION GNSS 2007)*, Fort Worth, TX, 1515–1529. https://doi.org/10.1002/j.2161-4296.2008.tb00415.x

Beck, F. C., Enneking, C., Oezmaden, C., Thoelert, S., & Meurer, M. (2024a). Multiple access interference challenges in GNSS: The role of emerging LEO-PNT constellations. *11th Workshop on Satellite Navigation Technology (NAVITEC 2024)*. https://elib.dlr.de/212952/

Beck, F. C., Enneking, C., Thölert, S., & Antreich, F. (2022). Comparison of constant and non-constant envelope signals for satellite navigation. *2022 10th Workshop on Satellite Navigation Technology (NAVITEC)*, 1–9. https://doi.org/10.1109/NAVITEC53682.2022.9847554

Beck, F. C., Enneking, C., Thölert, S., & Meurer, M. (2023). Galileo performance improvements employing meta-signals – Robustness analysis against payload and receiver distortions. *Engineering Proceedings*, *54*(1). https://doi.org/10.3390/enc2023-15472

Beck, F. C., Enneking, C., Thölert, S., & Meurer, M. (2024b). Optimized multilevel CDMA chip design with respect to payload and user constraints. *Proc. of the 37th International Technical Meeting of the Satellite Division of the Institute of Navigation (ION GNSS+ 2024)* (pp. 958–972). https://doi.org/10.33012/2024.19683

Betz, J. W. (2015). *Engineering satellite-based navigation and timing: Global navigation satellite systems, signals, and receivers* (J. W. Betz, Ed.). John Wiley & Sons, Inc. https://doi.org/10.1002/9781119141167

Betz, J. W., & Goldstein, D. B. (2002). Candidate designs for an additional civil signal in GPS spectral bands. *Proc. of the 2002 National Technical Meeting of the Institute of Navigation*, San Diego, CA, 622–631. https://www.mitre.org/publications/technical-papers/candidate-designs-for-an-additional-civil-signal-in-gps-spectral-bands

Betz, J. W., & Kolodziejski, K. R. (2009). Generalized theory of code tracking with an early-late discriminator part I: Lower bound and coherent processing. *IEEE Transactions on Aerospace and Electronic Systems*, *45*(4), 1538–1556. https://doi.org/10.1109/TAES.2009.5310316

Dassié, M., & Giorgi, G. (2021). Relativistic modelling for accurate time transfer via optical inter-satellite links. *Aerotecnica Missili & Spazio*, *100*(3), 277–288. https://doi.org/10.1007/s42496-021-00087-1

Enneking, C., Beck, F. C., Thölert, S., & Antreich, F. (2022). Transmit pulse shaping for 1-bit GNSS receivers. *Proc. of the 2022 International Conference on Localization and GNSS (ICL-GNSS)*, 01–06. https://doi.org/10.1109/ICL-GNSS54081.2022.9797019

Floch, J.-J., Issler, J.-L., Antreich, F., & Meurer, M. (2010). Comparison of different chip pulse shapes for DS-CDMA systems. *Proc. of the IEEE/ION Position, Location and Navigation Symposium,* Indian Wells, CA, 918–926. https://doi.org/10.1109/plans.2010.5507227

Giugno, L., & Luise, M. (2005). Optimum pulse shaping for delay estimation in satellite positioning. *Proc. of the 2005 13th European Signal Processing Conference*, 1–6. https://ieeexplore.ieee.org/document/7078061

Gold, R. (1967). Optimal binary sequences for spread spectrum multiplexing (corresp.) *IEEE Transactions on Information Theory*, *13*(4), 619–621. https://doi.org/10.1109/tit.1967.1054048

Hegarty, C., Betz, J. W., & Saidi, A. (2004a). Binary coded symbol modulations for GNSS. *Proc. of the 60th Annual Meeting of the Institute of Navigation*, Dayton, OH, 56–64. https://www.ion.org/publications/abstract.cfm?articleID=5597

Hegarty, C., Tran, M., & Betz, J. W. (2004b). Multipath performance of the new GNSS signals. *Proc. of the 2004 National Technical Meeting of the Institute of Navigation*, San Diego, CA, 333–342. https://www.ion.org/publications/abstract.cfm?articleID=5509

Hein, G. W., Ávila Rodríguez, J. Á., Ries, L., Lestarquit, L., Issler, J.-L., Godet, J., & Pratt, T. (2005). A candidate for the Galileo L1 OS optimized signal. *Proc. of the 18th International Technical Meeting of the Satellite Division of the Institute of Navigation (ION GNSS 2005)*, Long Beach, CA, 833–845. https://www.ion.org/publications/abstract.cfm?articleID=6279

ITU-R M.1831-1. (2015). International Telecommunication Union (ITU). https://www.itu.int/dms_pubrec/itu-r/rec/m/R-REC-M.1831-1-201509-I!!PDF-E.pdf

Kaplan, E. D., & Hegarty, C. J. (2005). *Understanding GPS principles and applications* (E. D. Kaplan & C. J. Hegarty, Eds.; 2nd ed.). Artech House, Inc. https://ieeexplore.ieee.org/document/9106073

Ma, J., Yang, Y., Li, H., & Li, J. (2020). Expressions for the autocorrelation function and power spectral density of BOC modulation based on convolution operation. *Mathematical Problems in Engineering*, *2020*, 1–12. https://doi.org/10.1155/2020/2063563

Miettinen, K. (1998). *Nonlinear multiobjective optimization* (F. S. Hillier, Ed.; 1st ed.). Springer New York, NY. https://doi.org/10.1007/978-1-4615-5563-6

Nocedal, J., & Wright, S. J. (2006). *Numerical optimization* (2nd ed.). Springer Science & Business Media. https://doi.org/10.1007/978-0-387-40065-5

Pratt, A. R., & Owen, J. I. R. (2003). BOC modulation waveforms. *Proc. of the 16th International Technical Meeting of the Satellite Division of the Institute of Navigation (ION GPS/GNSS 2003)*, Portland, OR, 1044–1057. https://www.ion.org/publications/abstract.cfm?articleID=5282

Pratt, A. R., & Owen, J. I. R. (2004). Performance of GPS/Galileo receivers using m-PSK BOC signals. *Proc. of the 2004 National Technical Meeting of the Institute of Navigation*, San Diego, CA, 362–370. https://www.ion.org/publications/abstract.cfm?articleID=5512

Rapp, C. (1991). Effects of HPA-nonlinearity on a 4-DPSK/OFDM-signal for a digital sound broadcasting system. *Second European Conference on Satellite Communications (ECSC-2),* Liege, Belgium, 179–184. https://elib.dlr.de/33776/

Rebeyrol, E. (2007). *Optimisation des signaux et de la charge utile Galileo* [Doctoral dissertation, Télécom ParisTech]. https://pastel.hal.science/pastel-00004315/

Rebeyrol, E., Macabiau, C., Julien, O., Ries, L., Issler, J.-L., Bousquet, M., & Boucheret, M.-L. (2006). Signal distortions at GNSS payload level. *Proc. of the 19th International Technical Meeting of the Satellite Division of the Institute of Navigation (ION GNSS 2006)*, Fort Worth, TX, 1595–1605. https://www.ion.org/publications/abstract.cfm?articleID=6850

Reid, T. G. R., Neish, A. M., Walter, T., & Enge, P. K. (2018). Broadband LEO constellations for navigation: Broadband LEOs for navigation. *NAVIGATION*, *65*(2), 205–220. https://doi.org/10.1002/navi.234

Schuldt, T., Gohlke, M., Oswald, M., Wüst, J., Blomberg, T., Döringshoff, K., Bawamia, A., Wicht, A., Lezius, M., Voss, K., Krutzik, M., Herrmann, S., Kovalchuk, E., Peters, A., & Braxmaier, C. (2021). Optical clock technologies for global navigation satellite systems. *GPS Solutions*, *25*(3). https://doi.org/10.1007/s10291-021-01113-2

Sharma, H., Dötterböck, D., & Pany, T. (2024). Assessment of potential system interference through radio frequency compatibility analysis on existing GNSS frequencies by emerging LEO constellations. *Proc. of the 2024 International Technical Meeting of the Institute of Navigation,* Long Beach, CA, 490–504. https://doi.org/10.33012/2024.19555

Thölert, S., Steigenberger, P., Montenbruck, O., & Meurer, M. (2019). Signal analysis of the first GPS III satellite. *GPS Solutions*, *23*(4), 1–11. https://doi.org/10.1007/s10291-019-0882-7

Vergara, M., & Antreich, F. (2012). Staggered interplex. *Proc. of the 2012 IEEE/ION Position, Location and Navigation Symposium*, Myrtle Beach, SC, 913–918. https://doi.org/10.1109/PLANS.2012.6236834

Vergara, M., Antreich, F., Enneking, C., Sgammini, M., & Seco-Granados, G. (2019). A model for assessing the impact of linear and nonlinear distortions on a GNSS receiver. *GPS Solutions*, *24*(1), 5. https://doi.org/10.1007/s10291-019-0917-0

Yao, Z., Guo, F., Ma, J., & Lu, M. (2017). Orthogonality-based generalized multicarrier constant envelope multiplexing for DSSS signals. *IEEE Transactions on Aerospace and Electronic Systems*, *53*(4), 1685–1698. https://doi.org/10.1109/taes.2017.2671580

Zhang, X., Yao, Z., & Lu, M. (2011a). Optimizing the Gabor bandwidth of satellite navigation signals by MCS signal expression. *Science China Physics, Mechanics and Astronomy*, *54*(6), 1077–1082. https://doi.org/10.1007/s11433-011-4329-6

Zhang, X., Yao, Z., Zhang, X., & Lu, M. (2011b). A method to optimize the spreading code chip waveform in sense of Gabor bandwidth. *Proc. of the 24th International Technical Meeting of the Satellite Division of the Institute of Navigation (ION GNSS 2011)*, Portland, OR, 1299–1304. https://www.ion.org/publications/abstract.cfm?articleID=9687

How to cite this article: Beck, F. C., Enneking, C., Thölert, S., & Meurer, M. (2026). Distortion-aware multilevel coded spreading symbol optimization for future navigation signals. *NAVIGATION, 73*. https://doi.org/10.33012/navi.740

A | ACF EXPRESSION OF MCS WAVEFORMS

The ACF and PSDs of currently broadcast GNSS signals can be clearly described as a sum of functions yielding an analytic expression (Ma et al., 2020). MCS waveforms are a generalized version of most broadcast GNSS signals. Assuming ideal properties for the range code ACF, the ACF of an MCS waveform is merely a superposition of weighted and time-shifted triangle functions:

$$R(\tau,\boldsymbol{w}_l)=\int_{-\infty}^{+\infty}p(t,\boldsymbol{w}_l)p^*(t-\tau,\boldsymbol{w}_l)\mathrm{d}t\int_{-\infty}^{+\infty}\left(\sum_{m=1}^{N_{\mathrm{sc}}}w_{lm}\sqcap_m(t)\right)\left(\sum_{n=1}^{N_{\mathrm{sc}}}w_{ln}\sqcap_n(t-\tau)\right)\mathrm{d}t \quad (27a)$$

$$=\sum_{m=1}^{N_{\mathrm{sc}}}\sum_{n=1}^{N_{\mathrm{sc}}}w_{lm}w_{ln}\int_{-\infty}^{+\infty}\sqcap_m(t)\sqcap_n(t-\tau)\mathrm{d}t=\sum_{m=1}^{N_{\mathrm{sc}}}\sum_{n=1}^{N_{\mathrm{sc}}}w_{lm}w_{ln}\triangle\left(\frac{\tau-(m-n)T_{\mathrm{sc}}}{T_{\mathrm{sc}}}\right) \quad (27b)$$

$$=\sum_{n'=-N_{\mathrm{sc}}+1}^{+N_{\mathrm{sc}}-1}\upsilon_{ln'}\triangle\left(\frac{\tau-n'T_{\mathrm{sc}}}{T_{\mathrm{sc}}}\right)\triangleq\sum_{n'=-N_{\mathrm{sc}}+1}^{+N_{\mathrm{sc}}-1}\upsilon_{ln'}\triangle_{n'} \quad (27c)$$

$$\triangle(t)=\begin{cases}1+t & -1\mathrm{s}<t\le 0\mathrm{s}\\ 1-t & +1\mathrm{s}>t>0\mathrm{s}\\ 0 & \text{else}\end{cases} \quad (28)$$

since:

$$\triangle(\tau)=\int_{-\infty}^{+\infty}\sqcap(t)\sqcap^*(t-\tau)\mathrm{d}t \quad (29)$$

By reducing the double sum to a single sum by defining the accumulated weights, we obtain the following:

$$\upsilon_{ln'} = \sum_{\substack{(m,n)\in\mathcal{N}^2 \\ n'=m-n}} w_{lm} w_{ln} \tag{30}$$

with the shift parameter $n' \in \{-N_{\mathrm{sc}}+1,\ldots,+N_{\mathrm{sc}}-1\}$.

B | PSD EXPRESSION OF MCS WAVEFORMS

The PSD of a multilevel CDMA chip can be obtained by applying the Wiener–Khinchin theorem to the result of the ACF, as explored by Ma et al. (2020), yielding the following:

$$G(f,\boldsymbol{w}_l) = \int_{-\infty}^{+\infty} R(\tau,\boldsymbol{w}_l) e^{-j2\pi f\tau} \mathrm{d}\tau = \tag{31a}$$

$$= \sum_{n'=-N_{\mathrm{sc}}+1}^{+N_{\mathrm{sc}}-1} \upsilon_{ln'} \int_{-\infty}^{+\infty} \Delta\left(\frac{\tau - n'T_{\mathrm{sc}}}{T_{\mathrm{sc}}}\right) e^{-j2\pi f\tau} \mathrm{d}\tau = \tag{31b}$$

$$= T_{\mathrm{sc}} \sum_{n'=-N_{\mathrm{sc}}+1}^{+N_{\mathrm{sc}}-1} \upsilon_{ln'} \operatorname{sinc}^2(T_{\mathrm{sc}} f) e^{-j2\pi f n' T_{\mathrm{sc}}} \tag{31c}$$

where $\operatorname{sinc}(x) := \sin(\pi x)/(\pi x)$ denotes the normalized sinc function. The PSD expression is used to evaluate the SSC of an MCS with itself or other interference victims.

C | GBO MCS

In a setup without distortion, Zhang et al. (2011a) showed that the MCS for a two-sided front-end target bandwidth B, with a subchip number N_{sc} and chip duration $T_{\mathrm{c}} = N_{\mathrm{sc}} T_{\mathrm{sc}}$, that maximizes the Gabor bandwidth:

$$\beta_{\mathrm{rms}} = \sqrt{\frac{1}{\eta_l} \int_{-B/2}^{+B/2} f^2 G(f,\boldsymbol{w}_l) \mathrm{d}f} \tag{32}$$

can be found by solving the equivalent eigenvalue problem:

$$\boldsymbol{A}\boldsymbol{w}_l = \lambda \boldsymbol{w}_l \tag{33}$$

for the eigenvector with the largest eigenvalue. Here, we have the following:

$$\boldsymbol{A} = \int_{-B/2}^{+B/2} f^2 G_{\mathrm{sc}}(f,T_{\mathrm{sc}}) \boldsymbol{v}\boldsymbol{v}^H \mathrm{d}f \in \mathbb{C}^{N_{\mathrm{sc}}\times N_{\mathrm{sc}}} \tag{34}$$

which denotes the Gabor bandwidth contribution matrix with the pulse base PSD $G_{\mathrm{sc}}(f,T_{\mathrm{sc}}) = T_{\mathrm{sc}} \operatorname{sinc}^2(T_{\mathrm{sc}} f)$ and the following frequency shift vector:

$$\boldsymbol{v} = \begin{bmatrix} e^{j2\pi f T_{\mathrm{sc}}} & e^{j2\pi f T_{\mathrm{sc}} 2} & \cdots & e^{j2\pi f T_{\mathrm{sc}} n} & \cdots & e^{j2\pi f T_{\mathrm{sc}}(N_{\mathrm{sc}}-1)} & e^{j2\pi f T_{\mathrm{sc}} N_{\mathrm{sc}}} \end{bmatrix}^{\mathrm{T}} \in \mathbb{C}^{N_{\mathrm{sc}}\times 1} \tag{35}$$

which yields the GBO MCS. In this study, GBO MCSs with $N_{\mathrm{sc}} = 10$, $T_{\mathrm{c}} = T_{\mathrm{b}}/10$, and target front-end bandwidths B are compared with distortion-aware MCSs.